A new plastic flow theoretical model and verification for non-dense metals

Dan Qiao, Bao Yang, Zhenyu Jiang, Licheng Zhou[*], Zejia Liu, Yiping Liu, and Liqun Tang[*]

School of Civil Engineering and Transportation, State Key Laboratory of Subtropical Building Science, South China University of Technology, Guangzhou 510640, China

The mechanical behavior and constitutive equations of isotropic non-dense metals, such as metal foams, porous metals, and lattice metals, have been extensively studied, but the subsequent yield surfaces depicted by different theoretical models are somewhat controversial and have not been fully validated in the whole permissible loading space. Based on two accepted assumptions for isotropic non-dense metals, we proposed a new plastic flow theoretical model. In order to verify its rationality, we established two mesoscopic models with different initial relative densities and different meso-structures. Then, the large amount of numerical simulation experimental data was established, which covers enough multiaxial loadings in the permissible principle-strain space. Our model solves some of the controversies in current models and adapts the equivalent stress, equivalent strain, and constitutive equations seamlessly to deformation from non-dense to dense state. Numerical results from two mesoscopic models show the relations between equivalent stress and plastic strain in our theoretical model have better consistency under all multiaxial loadings than those in some known models. We checked the topology of subsequent yield surfaces in the plastic principle-strain space and the results turn out the subsequent yield surfaces are not self-similar. The large amount of numerical test data not only well validates our theoretical model but also will be beneficial to the mechanical study of non-dense metals under multiaxial loadings.

Isotropic non-dense metals, Plastic theoretical model, Equivalent stress, Equivalent strain, Subsequent yield surface

1. Introduction

The mechanical behavior and constitutive equations of isotropic non-dense metals, such as metal foams, porous metals, and lattice metals, have been extensively studied [1-5], several constitutive equations and subsequent yield surface equations of non-dense metals have been developed [6,7]. Different from the traditional metals, non-dense metals have obvious volume compressibility [8-10], so the constitutive models of dense metals cannot be directly applied to non-dense metals. In practical engineering applications, non-dense metals are mostly subjected to complex multiaxial compression loads [11-13], and the deformation mechanism under multiaxial loads is complex [14-17]. However, the existing theoretical models of non-dense metals are somewhat controversial [6,18,19], and have not been fully validated in the permissible loading space due to the difficulty of carrying out multiaxial experiments [8,11,12]. Therefore, we proposed a new plastic flow theoretical model to solve the controversies among current models, and established two mesoscopic models with different relative densities to verify the rationality of our theoretical model.

1.1 Plastic theory of traditional metals

The plasticity theory of traditional metals has been developed for a long time and is now quite well developed. At the beginning, Tresca [20] found that metal materials would exhibit some fluidity under certain stress conditions. On this

basis, de Saint-Venant [21] proposed the famous Saint-Venant principle with reference to fluid viscosity for plane problems. Lévy [22] transformed plane problems into space problems. Then, the yield theory of metal materials gradually emerged, the most classic model is the Mises yield criterion [23], which uses the Mises stress σ_e to represent the yield criterion of metals, $\sigma_e = \sqrt{3\mathbf{ss}/2}$, and $\mathbf{s}$ is the deviatoric stress tensor. Later, the Prandtl-Reuss equations [24,25] distinguished between elastic deformation and plastic deformation, the equations can be written as

$$\boldsymbol{\sigma} = \lambda \varepsilon_{kk}^{e} \boldsymbol{\delta} + 2\mu \boldsymbol{\varepsilon}^{e}, \tag{1a}$$

$$\dot{\mathbf{e}}^{p} = \dot{C}\mathbf{s}, \tag{1b}$$

where λ and μ are Lame's constants, $\boldsymbol{\sigma}$ is the stress tensor, $\boldsymbol{\delta}$ is the unit tensor, $\boldsymbol{\varepsilon}^{e}$ is the elastic strain tensor, $\dot{\mathbf{e}}^{p}$ is the deviatoric plastic strain rate tensor, and C is the plastic flexibility of metals determined experimentally, the over-dot of a variable represents the differentiate of the variable with respect to time, and the superscripts e or p respectively represent the variable is related to the elastic part or plastic part of the strain tensor. The Drucker-Prager postulate [26] is referred to the plastic flow rule, which is commonly used in the constitutive models of metals and non-dense metals [19,27], and it is divided into associated type and non-associated type according to whether the yield surface is defined as the flow potential function.

Based on the previous theoretical research, the plasticity theory of traditional metals contains two basic assumptions:

(1) Only existing plastic distortion deformation and no plastic volumetric deformation;

(2) Decoupling of distortion deformation law and volumetric deformation law: plastic distortion deformation is related to deviatoric stress only, and nothing to do with mean stress.

For isotropic non-dense metals, it is clear that the first assumption cannot be applied due to the abundance of internal cell structures, which indicates that the plasticity properties are both influenced by the deviatoric stress and mean stress.

1.2   Yield surfaces of isotropic non-dense metals

As one of common isotropic non-dense metals, metal foams have the advantages of low cost, easy manufacture, and wide application scenarios, so the plasticity properties were widely studied, especially the initial yield surface and subsequent yield surface [28,29]. The yield surfaces of metal foams are usually observed in the mean stress and Mises stress plane [7], and the shape is mainly divided into parabolic type [8,9,28] and elliptical type [7,30]. The typically parabolic type is the GAZT model proposed by Gibson et al. [8,28]. The most classic model of the elliptical type is the self-similar model proposed by Deshpande and Fleck [7],

usually called the D-F model, the equations are as follows:

$$\Phi \equiv \bar{\sigma} - T \leq 0,$$
$$\bar{\sigma}^{2} = \frac{1}{1+(\alpha/3)^{2}}\left(\sigma_e^{2} + \alpha^{2}\sigma_m^{2}\right),$$
$$\left(\bar{\varepsilon}^{p}\right)^{2} = \left[1+(\alpha/3)^{2}\right]\left[\left(\dot{\varepsilon}_e^{p}\right)^{2} + \frac{1}{\alpha^{2}}\left(\dot{\varepsilon}_m^{p}\right)^{2}\right], \tag{2}$$
$$\dot{\bar{\sigma}} = \left[\frac{\sigma_e}{\bar{\sigma}}H_u + \left(1 - \frac{\sigma_e}{\bar{\sigma}}\right)H_t\right]\dot{\bar{\varepsilon}}^{p},$$

where $\bar{\sigma}$ is the equivalent stress, σ_m is the mean stress, $\sigma_m = \sigma_{kk}/3$, $\bar{\varepsilon}^{p}$ is the equivalent plastic strain, $\dot{\varepsilon}_e^{p}$ is the Mises plastic strain rate, $\dot{\varepsilon}_e^{p} = \sqrt{2\dot{\mathbf{e}}^{p}\dot{\mathbf{e}}^{p}/3}$, $\dot{\varepsilon}_m^{p}$ is the volumetric plastic strain rate, $\dot{\varepsilon}_m^{p} = \dot{\varepsilon}_{kk}^{p}$, and the ellipticity α is obtained from the shape of yield surfaces, H_u and H_t are the hardening modulus obtained from uniaxial compression and triaxial equal-proportion loading conditions. In the D-F model, the associated flow rule is adopted and the subsequent yield evolution is controlled by function T which is related to the equivalent plastic strain $\bar{\varepsilon}^{p}$. Chen and Lu [31] proposed the yield surface equation combined with equivalent stress and associated plastic flow rule:

$$\Phi = \bar{\sigma}^{2} + \Phi_1\left(\bar{\varepsilon}, \sigma_{ij}\right) - T(\bar{\varepsilon}). \tag{3}$$

Of course, if $\Phi_1\left(\bar{\varepsilon}, \sigma_{ij}\right) = 0$, Eq. (3) can be degenerated into the D-F model. Forest et al. [30] defined the following Eq. (4), which was similar to the equivalent stress equation in the D-F model:

$$\bar{\sigma}^{2} = F\sigma_e^{2} + G\sigma_m^{2}, \tag{4}$$

where the parameters F and G are assumed to depend on porosity, but lack clear physical significance.

The D-F model is widely used because of the simplicity and few parameters, while due to the lack of sufficient experimental data, Fleck thought that the ellipticity α in Eq. (2) always remains constant during the subsequent yield evolution process, which has been questioned by subsequent scholars. Some scholars had further modified the ellipticity on the basis of the D-F model and believed [6,7,32] the ellipticity α and plastic Poisson's ratio v^{p} have the relation $\alpha^{2} = 9(1-2v^{p})/[2(1+v^{p})]$, but the plastic Poisson's ratio v^{p} is difficult to measure in practice, so different researches gave scattered values of the ellipticity [7,17,32]. Zhu et al. [6] pointed out there was a problem with that the ellipticity was assumed to be constant, and proposed the ellipticity changed with equivalent plastic strain, called the Zhu-Zheng model:

$$\alpha^{2} = b_1\exp\left(-b_2\bar{\varepsilon}^{p}\right) + b_3(\bar{\varepsilon}^{p})^{2} + b_4, \tag{5}$$

where b_1, b_2, b_3, b_4 are the phenomenological parameters obtained from several multiaxial loading conditions. However, in the Zhu-Zheng model, the definitions of ellipticity α

and equivalent plastic strain $\bar{\varepsilon}^p$ affect each other, and there is a lack of discussion on the physical significance of the ellipticity. Recently, Zhuang et al. [18] revised the D-F model again through the plastic Poisson's ratio observed by DIC and the modified ellipticity, but only the uniaxial compression and hydrostatic pressure conditions were considered, which was not convincing enough. Besides, some scholars thought Lode parameters affected the shapes of yield surfaces [33,34]. While Wu et al. [19] found that the Lode parameters had less influence and the tension-compression asymmetry was not obvious on the initial yield surface according to the complete shape in the principle-strain space.

To sum up, some scholars believe the ellipticity in the constitutive models is not constant, but have not given a clear physical significance to it, so the definitions of equivalent stress and equivalent strain are also not reasonable enough. Furthermore, the topology of subsequent yield surfaces is controversial, and has not been checked in the principle-strain space due to the lack of sufficient experimental data.

1.3　Mesoscopic models for predicting the mechanical behavior of non-dense metals

Due to the difficulty of carrying out multiaxial experiments, more and more scholars obtained the mechanical behavior under multiaxial loads through numerical simulation experiments [35-37]. In the numerical simulation experiment, firstly, a multicellular geometric model similar to the cellular material was constructed, and the geometric model was endowed with the same material properties with matrix material, then multiaxial loads were applied to the geometric model to obtain the mechanical properties. The commonly used simulation mesoscopic models are mainly divided into three types according to different meso-structures [38]: regular meso-structures [39,40], three-dimensional (3D) CT-based meso-structures [41-43] and Voronoi meso-structures [44,45]. In regular meso-structure models, the cellular pores are usually spherical structures [46], hexahedrons and decahedrons, etc. Among them, the spherical structure is the simplest and satisfies strong isotropy. Currently, the popular metal foams are isotropic non-dense metals with low relative density [8], and the mesoscopic modeling methods of metal foams include: (1) the CT-based model scans the real metal foams through 3D CT, and establishes a model whose mesoscopic structure is similar to the metal foams. But the modeling process of CT-based model is too complicated and the amount of calculation is large; (2) Voronoi mesoscopic model uses the 3D Voronoi method to establish a geometric model with a random cell structure and controls the relative density through shell element parameters [47], and the calculation amount is relatively small, so the Voronoi meso-

scopic model is widely used. Tang et al. [48] used the Voronoi mesoscopic model to statistically calculate the effect of shape irregularity and size irregularity of cell structures on the mechanical properties of metal foams under uniaxial loading condition. Zhang et al. [3,49] analyzed the influence of different meso-structural parameters under multiaxial loads, and preliminarily tested the validity of the Voronoi mesoscopic model through uniaxial tension and compression experiments. On this basis, Wu et al. [19,50] further verified the validity through biaxial tensile experiments, and gave the complete initial yield surface and failure surfaces of metal foams in the principle-strain space.

To sum up, the spherical regular meso-structure is more uniform and the relative density is high. The Voronoi mesoscopic model has certain randomness and the relative density can be low. In order to verify the rationality of our theoretical model, we considered to establish two mesoscopic models with different initial relative densities and different meso-structures.

1.4　Main works in this paper

(1) Starting from the plasticity theory of conventional metals, two basic plasticity assumptions of non-dense metals were clarified. On this basis, a new plastic flow theoretical model of isotropic non-dense metals was proposed to solve the controversies among current theoretical models.

(2) In order to verify its rationality, we established two mesoscopic models with different initial relative densities and different meso-structures, namely the isotropic spherical cell model and Voronoi mesoscopic model. Then, the large amount of numerical simulation experimental data was established, which covers enough multiaxial loadings in the permissible principle-strain space.

(3) Then, the numerical results were analyzed, and found that the relations between equivalent stress and strain in our theoretical model have good consistency under all multiaxial loadings than those in some known models. And our model adapts the equivalent stress, equivalent plastic strain, and constitutive equations seamlessly to deformation from non-dense to dense state.

(4) Finally, we checked the topology of subsequent yield surfaces in the plastic principle-strain space, and the results turn out that the subsequent yield surfaces are not self-similar.

2.　Theoretical model

To solve the controversies among current theoretical models we proposed a new plastic flow theoretical model for isotropic non-dense metals. Based on the assumptions of isotropic non-dense metals, we gave the extended Prandtl-

Reuss equations and constructed two constitutive equations to close the set of constitutive equations.

2.1 Extended Prandtl-Reuss equations

The presence of plastic volumetric deformation is the main difference between non-dense metals and dense metals. And common non-dense metals such as metal foams are considered to satisfy macroscopic isotropy [7,9]. Combining these two features, two basic assumptions of non-dense metals were clarified:

Assumption 1: Both existing plastic distortion deformation and plastic volumetric deformation;

Assumption 2: Decoupling of distortion deformation law and volumetric deformation law: plastic distortion deformation is only related to deviatoric stress, and plastic volumetric deformation is only related to mean stress.

According to the above assumptions, the plastic flexibility C (in Eq. (1b)) of initial dense metal is classified into plastic distortion flexibility C_e and plastic volume flexibility C_m, which characterize the relationships between deviatoric stress and deviatoric plastic strain, mean stress and volumetric plastic strain respectively:

$$\dot{\mathbf{e}}^{p} = \dot{C}_e \mathbf{s}, \tag{6a}$$

$$\dot{\varepsilon}_m^{p} = \dot{C}_m \sigma_m, \tag{6b}$$

where $\dot{\varepsilon}_m^{p} = \dot{\varepsilon}_{kk}^{p}$ and $\sigma_m = \sigma_{kk}/3$, $\dot{C}_e$ is the plastic distortion-flexibility rate and $\dot{C}_m$ is the plastic volume-flexibility rate. Combining Eqs. (1) and (6), the extended Prandtl-Reuss equations for isotropic non-dense metals were proposed as

$$\dot{\boldsymbol{\varepsilon}}^{e} + \dot{\boldsymbol{\varepsilon}}^{p} = \dot{\boldsymbol{\varepsilon}}, \quad \dot{\boldsymbol{\varepsilon}}^{p} = \dot{\mathbf{e}}^{p} + \dot{\varepsilon}_{kk}^{p}\boldsymbol{\delta}/3,$$
$$\dot{\mathbf{s}} = \dot{\boldsymbol{\sigma}} - \dot{\sigma}_{kk}\boldsymbol{\delta}/3, \quad \dot{\boldsymbol{\sigma}} = \lambda\dot{\varepsilon}_{kk}^{e}\boldsymbol{\delta} + 2\mu\dot{\boldsymbol{\varepsilon}}^{e}, \tag{7}$$
$$\dot{\mathbf{e}}^{p} = \dot{C}_e\mathbf{s}, \quad \dot{\varepsilon}_{kk}^{p} = \dot{C}_m\sigma_{kk}/3,$$

where $\boldsymbol{\varepsilon}$ is the strain tensor. In fact, the plastic flow rule has already been considered in Eq. (7), because the orthogonally and fluidity are guaranteed by the plastic distortion flexibility and plastic volume flexibility. The extended Prandtl-Reuss equations are the flow constitutive equations applicable to isotropic non-dense metals and do not depend on the existence of stress-strain relations or yield surfaces [51], so we constructed the theoretical model on the basis of them.

For spatial displacement-loading problems, $\dot{\boldsymbol{\varepsilon}}$ is a known tensor, and the tensor expressions in the extended Prandtl-Reuss equations all contain 6 equations or unknowns, while according to the characteristics of deviatoric stress and deviatoric plastic strain rate ($s_{kk} = 0$ and $\dot{e}_{kk}^{p} = 0$), there are only 5 independent equations or unknowns when $\mathbf{s}$ or $\dot{\mathbf{e}}^{p}$ is contained in expressions. The independent equations and unknowns in the extended Prandtl-Reuss equations were listed in Table 1, and there are a total of 28 independent

equations and 30 unknown variables.

From Table 1, we need to construct two additional constitutive equations to obtain a closed set of constitutive equations, but the directly constructing method of constitutive equations from σ_m, σ_e or C_m, C_e is still difficult, because the governing equations related to yield surfaces are unknown. That is why researchers usually tend to define equivalent stress and equivalent plastic strain (or equivalent strain) [6,7], so we followed this train of thought to define the reasonable equivalent stress and equivalent plastic strain firstly, which are directly related to the subsequent yield surfaces.

In addition, for force-loading problems, the known variables change from $\dot{\boldsymbol{\varepsilon}}$ to $\dot{\boldsymbol{\sigma}}$, and the numbers of independent equations and unknown variables keep no change. For dense metals, $\dot{\varepsilon}_{kk}^{p} \equiv 0$ and the equation $\dot{\varepsilon}_{kk}^{p} = \dot{C}_m\sigma_{kk}/3$ becomes $C_m = 0$, so there is only one additional constitutive equation needed to be added.

2.2 Equivalent stress and equivalent plastic strain

For isotropic non-dense metals, the relations of plastic dissipation power and equivalent stress and plastic strain usually meet $P = \overline{\sigma}\dot{\overline{\varepsilon}}^{p}$. After transforming form and introducing the dimensionless function A (The specific process is shown in Appendix A), the equivalent stress and equivalent plastic strain were given as

$$(\overline{\sigma})^2 = A\left(2\sigma_e^2/3 + \sigma_m^2\dot{C}_m/\dot{C}_e\right),$$
$$(\overline{\varepsilon}^{p})^2 = \frac{1}{A}\left[3\left(\dot{e}_e^{p}\right)^2/2 + \left(\dot{\varepsilon}_m^{p}\right)^2\dot{C}_e/\dot{C}_m\right]. \tag{8}$$

The specific expressions of Eq. (8) are very close to these of the D-F like models, so the parameters in different theoretical models can be compared. The ellipticity α in Eq. (2) can be defined as Eq. (9) and has more clear physical significance: it is the ratio of the plastic volume-flexibility rate to the plastic distortion-flexibility rate:

$$\alpha^2 = 3\dot{C}_m/\left(2\dot{C}_e\right). \tag{9}$$

In the D-F model, the ellipticity α was regarded as a

Table 1 Number of independent equations and unknowns in the extended Prandtl-Reuss equations

Equations	Number of independent equations	Unknowns	Number of unknowns
$\dot{\varepsilon}^{e} + \dot{\varepsilon}^{p} = \dot{\varepsilon}$	6	$\boldsymbol{\varepsilon}^{e}$	6
$\boldsymbol{\varepsilon}^{p} = \mathbf{e}^{p} + \boldsymbol{\varepsilon}_{kk}^{p}\boldsymbol{\delta}/3$	5	$\boldsymbol{\varepsilon}^{p}$	6
$\dot{\mathbf{s}} = \dot{\boldsymbol{\sigma}} + \boldsymbol{\sigma}_{kk}\boldsymbol{\delta}/3$	5	$\dot{\mathbf{s}}$	5
$\boldsymbol{\sigma} = \lambda\boldsymbol{\varepsilon}_{kk}^{e}\boldsymbol{\delta} + 2\mu\boldsymbol{\varepsilon}^{e}$	6	$\boldsymbol{\sigma}$	6
$\dot{\mathbf{e}}^{p} = \dot{C}_e\mathbf{s}$	5	$\dot{\mathbf{e}}^{p}, C_e$	5 + 1
$\dot{\varepsilon}_{kk}^{p} = \dot{C}_m\sigma_{kk}/3$	1	C_m	1
Total	28	–	30

constant under arbitrary loading conditions for metal foams. But according to Eq. (9), it is a parameter related to two deformation rates and cannot be a constant, for example, a "pure" distortion deformation may induce ellipticity α to zero. That is why many researchers try to modify α and relate it to the material deformation. Similarly, the coefficients F and G in Eq. (4) can also be represented by $\dot{C}_e$ and $\dot{C}_m$, which means that the coefficients are given clear physical significance.

At present, the function A is the key to determining our equivalent stress and equivalent plastic strain equations. Based on our previous knowledge of metal foams, there are two facts:

(1) The shape irregularity of metal foams has a non-negligible impact on the constitutive relationship [52], including the yield surface. And the greater shape irregularity, the lower yield stress;

(2) The relative density of metal foams significantly affects the yield surface [3]. And the larger the relative density, the larger the yield stress.

The shape irregularity corresponds to the distortion deformation at the macroscopic level, which can be represented by $\varepsilon_e^{\,p}$, and the current relative density [53] can be represented by $\varepsilon_m^{\,p}$. Considering relative density and shape irregularity have opposite effects on the stress and referring to the ellipticity α in the D-F like models, we believe that A should be a function of $\varepsilon_e^{\,p}/\varepsilon_m^{\,p}$ and $\dot{C}_m/\dot{C}_e$. In addition, in order to make function A more versatile, it should meet three basic requirements: (1) it can be directly used for initial dense metals ($\dot{C}_m/\dot{C}_e \equiv 0$); (2) it can adapt to the deformation from non-dense to dense; (3) it does not diverge under hydrostatic loads. Based on these three requirements, we choose a simple expression—the linear combination of the power functions of $\dot{C}_m/\dot{C}_e$ and $\varepsilon_e^{\,p}/\varepsilon_m^{\,p}$, as the following equation:

$$A = \frac{a\left[\dot{C}_m/\dot{C}_e + b\left(\varepsilon_e^{\,p}/\varepsilon_m^{\,p}\right)^d\right]}{\dot{C}_m/\dot{C}_e + c\left(\varepsilon_e^{\,p}/\varepsilon_m^{\,p}\right)^d}. \tag{10}$$

Substituting Eq. (10) into Eq. (8), the specific equations of equivalent stress and equivalent plastic strain can be obtained:

$$(\overline{\sigma})^2 = \frac{a\left[\dot{C}_m/\dot{C}_e + b\left(\varepsilon_e^{\,p}/\varepsilon_m^{\,p}\right)^d\right]}{\dot{C}_m/\dot{C}_e + c\left(\varepsilon_e^{\,p}/\varepsilon_m^{\,p}\right)^d}\left(2\sigma_e^2/3 + \sigma_m^2\dot{C}_m/\dot{C}_e\right),$$

$$(\dot{\overline{\varepsilon}}^{\,p})^2 = \frac{\dot{C}_m/\dot{C}_e + c\left(\varepsilon_e^{\,p}/\varepsilon_m^{\,p}\right)^d}{a\left[\dot{C}_m/\dot{C}_e + b\left(\varepsilon_e^{\,p}/\varepsilon_m^{\,p}\right)^d\right]}\left[3(\dot{\varepsilon}_e^{\,p})^2/2 + (\dot{\varepsilon}_m^{\,p})^2\dot{C}_e/\dot{C}_m\right]. \tag{11}$$

Equation (11) contains four constant coefficients, the coefficient a is a scale coefficient that can be obtained by referring to the loading curve of hydrostatic pressure condition, and c is a small number $c = 0.001$, existing to prevent the denominator from being 0 under special cases. The coefficients b and d change with the initial relative densities of mesoscopic models, and affect the shapes of $\overline{\sigma}$-$\overline{\varepsilon}^{\,p}$ relations. After the equations of equivalent stress and equivalent plastic strain were determined, we further constructed the two additional constitutive equations to close the constitutive equations.

2.3 Additional constitutive equations

Since the equivalent stress and equivalent plastic strain have been recommended in Eq. (11), one constitutive equation can be set as the relation of them. As for the second constitutive equation, some researchers choose to set the relation of the ellipticity and equivalent plastic strain, such as Eq. (5). Here, according to the native feature of plastic volumetric deformation of non-dense metals, we simply choose the function of plastic volume-flexibility rate $\dot{C}_m$ against the deformation variables. So, the two constitutive equations are given following:

$$\dot{\overline{\sigma}} = \dot{\overline{\sigma}}(\overline{\varepsilon}^{\,p},\ \dot{\overline{\varepsilon}}^{\,p}), \tag{12a}$$

$$\dot{C}_m = \dot{C}_m\!\left(\varepsilon_m^{\,p},\ \varepsilon_e^{\,p}\right). \tag{12b}$$

Next, the two constitutive equations were discussed separately.

2.3.1 *Relative equation between equivalent stress and equivalent plastic strain*

Ideally, the optimal coefficients should result in a high concentration for the relations of equivalent stress and equivalent plastic strain under different proportion loading conditions. According to the relevant studies of metal foams [18], the shape of the hydrostatic pressure curve is basically close to that of uniaxial loading curve, so the specific form of Eq. (12a) can be characterized by referring to uniaxial theoretical models. Besides, Eq. (13) should meet the two requirements: (1) it will degenerate to linear for dense metals; (2) when the equivalent plastic strain rate keeps 0 ($\dot{\overline{\varepsilon}}^{\,p} \equiv 0$), the equivalent stress rate is 0 ($\dot{\overline{\sigma}} = 0$). The rate related expression of Eq. (12a) is given as

$$\dot{\overline{\sigma}} = a_1\dot{\overline{\varepsilon}}^{\,p}\!\left[1 + \exp\!\left(a_2\overline{\varepsilon}^{\,p}\right)\right], \tag{13}$$

where a_1 is related to the subsequent hardening, a_2 is related to the dense stage of materials. The specific values of a_1 and a_2 in Eq. (13) can be obtained from the hydrostatic pressure condition.

2.3.2 Relative equation between plastic volume flexibility and plastic strain

Similarly, the relative equation between plastic volume flexibility and plastic strain should meet the two requirements: (1) it contains the plastic triaxiality, and when the plastic triaxiality increases, the volume flexibility rate of the model should be reduced due to the ratio of volumetric deformation to whole deformation is gradually less; (2) it keeps 0 ($\dot{C}_m = 0$) for dense state ($\dot{\varepsilon}_m^p = 0$). Besides, referring to the equation for the plastic flexibility rate of dense metals (The equation is given in Appendix B), the plastic bulk flexibility of non-dense metals should satisfy the logarithmic form. Considering the above reasons, Eq. (14) was given as follows:

$$\dot{C}_m = \frac{a_3 \dot{\varepsilon}_m^p}{1 + a_4 \varepsilon_m^p \exp\left[a_5\left(\varepsilon_e^p / \varepsilon_m^p\right)^{a_6}\right]}. \tag{14}$$

The coefficients a_3, a_4, a_5, a_6 are constants related to materials, which need to be determined from triaxial loading conditions. Compared with Eq. (6b), Eq. (14) is basically equivalent to the expression of σ_m, which is obviously independent on the extended Prandtl-Reuss equations.

According to the above analysis, combined with Eqs. (7), (11), (13) and (14), the new plastic flow theoretical model is obtained, which gives a clear physical significance for the ellipticity and solves the controversies among current models.

2.4 Theoretical analysis under the extreme deformation process

To test the applicability of our model, we designed an extreme deformation process, which is compressing the non-dense metal to fully dense state. Obviously, the plastic volumetric strain will always be constant when loaded to dense, so we considered that the equivalent stress, equivalent strain, and constitutive equations have the following properties: the equivalent stress and equivalent plastic strain will degrade to be proportional to the Mises stress and Mises strain, respectively; the constitutive relations of equivalent stress and equivalent plastic strain do not change with different loading conditions, which means the equivalent stress is only related to the equivalent plastic strain; the plastic volume compliance constitutive equation becomes the identity.

Because the plastic volumetric deformation no longer increases, the volumetric plastic strain rate remains at 0, and the mean stress is not 0, so the plastic volume-flexibility rate $\dot{C}_m$ is 0 in any loading condition. The following equations exist:

$$\varepsilon_m^p = \text{const}, \ \dot{\varepsilon}_m^p = 0, \ \sigma_m \neq 0, \ \dot{C}_m = 0. \tag{15}$$

For the convenience of the comparison with the D-F model and the Zhu-Zheng model, combined with Eq. (15), we listed the constitutive equations of different theoretical models under the deformation process in Table 2.

From Table 2, only our theoretical model satisfies the equivalent stress, equivalent plastic strain, and constitutive equations adapt seamlessly to deformation from non-dense to dense state.

3. Verification methods and data processing

To verify the rationality of our theoretical model, we established two mesoscopic models and enough triaxial loading conditions in the permissible loading space. After the model verification and correction, the calculation process of $\overline{\sigma}$-$\overline{\varepsilon}^p$ relations could be given, and the dispersion value was proposed to facilitate the analysis and comparison of data.

3.1 Mesoscopic models

Two mesoscopic models with different initial relative densities and different meso-structures were established, namely the isotropic spherical cell model and the Voronoi mesoscopic model.

3.1.1 Isotropic spherical cell model

The isotropic spherical cell model is called Sph-cell model for convenience. We took a cube with a side length of 75 mm and uniformly dug out spheres with radius R = 5.7 mm to obtain the Sph-cell model with 60.3% relative density, as shown in Fig. 1b. The presence of 6 cells in one

Table 2 Comparison of different constitutive equations when a non-dense metal is loaded to fully dense

Our model	The D-F model	The Zhu-Zheng model
$\overline{\sigma}^2 = \dfrac{ab}{c}\dfrac{2}{3}\sigma_e^2$	$(\overline{\sigma})^2 = \dfrac{1}{1+(\alpha/3)^2}(\sigma_e^2 + \alpha^2\sigma_m^2)$	$(\overline{\sigma})^2 = \dfrac{1}{1+(\alpha/3)^2}(\sigma_e^2 + \alpha^2\sigma_m^2)$
$(\overline{\varepsilon}^p)^2 = \dfrac{c}{ab}\left[\dfrac{3}{2}(\dot{\varepsilon}_e^p)^2\right]$	$(\overline{\varepsilon}^p)^2 = [1+(\alpha/3)^2](\dot{\varepsilon}_e^p)^2$	$(\overline{\varepsilon}^p)^2 = [1+(\alpha/3)^2](\dot{\varepsilon}_e^p)^2$
$\overline{\sigma} = a_1\overline{\varepsilon}^p\left[1 + \exp(a_2\overline{\varepsilon}^p)\right]$	$\overline{\sigma} = \left[\dfrac{\sigma_e}{\overline{\sigma}}H_u + \left(1 - \dfrac{\sigma_e}{\overline{\sigma}}\right)H_t\right]\overline{\varepsilon}^p$	$\overline{\sigma} = \left[\dfrac{\sigma_e}{\overline{\sigma}}H_u + \left(1 - \dfrac{\sigma_e}{\overline{\sigma}}\right)H_t\right]\overline{\varepsilon}^p$
$\dot{C}_m = 0$	$\alpha = \text{const}$	$\alpha^2 = b_1\exp(-b_2\overline{\varepsilon}^p) + b_3(\overline{\varepsilon}^p)^2 + b_4$

single direction is enough to ensure the stability of the macroscopic mechanical properties of the mesoscopic model. The unidirectional profile of Sph-cell model in *Y* direction and the representative volume unit were shown in Fig. 1a and c, respectively.

3.1.2   Voronoi mesoscopic model

Then, the Voronoi mesoscopic model was established, as shown in Fig. 1e, which is the same with the models used in our previous studies [19,49,50], called Voronoi model here. The usability of Voronoi model had been verified in our previous researches. The initial relative density of Voronoi model is 13% and the model size is 30 mm × 30 mm × 30 mm. The average cell radius is about 1.66 mm, so there are about 9 cells in one direction, which can effectively keep the stability of the macroscopic mechanical properties. The unidirectional profile of Voronoi model in *Y* direction and the representative volume unit were shown in Fig. 1d and f.

The matrix materials of the mesoscopic models are metal aluminum with elastoplastic constitutive relationship. The elastic modulus is 70 GPa and the plastic hardening modulus

is 30 MPa. In practical and simulation experiments, force-loading and displacement-loading methods are usually used [3,6]. Due to the long stress plateau stage of cellular metals, the force-loading method is used for initial yield studies, and the displacement-loading method is more suitable for subsequent yielding studies. Therefore, we used the triaxial displacement-loading method to control the nominal strain rate of mesoscopic models. During the loading process, the six surfaces of mesoscopic model are fixed by rigid plates, the negative directions of *XYZ* axis are called fixed ends and the rigid plates at fixed ends remain stationary, the positive directions are called loading ends and the rigid plates at loading ends are controlled by displacement. The triaxial displacement-loading diagrams of Sph-cell model and Voronoi model were shown in Fig. 2a and b.

3.2   Loading conditions

Typically, cellular metals will fail under tension conditions and the failure points under different loading conditions together form the failure surface. According to Wu's researches [19,50], the distance between the failure surface
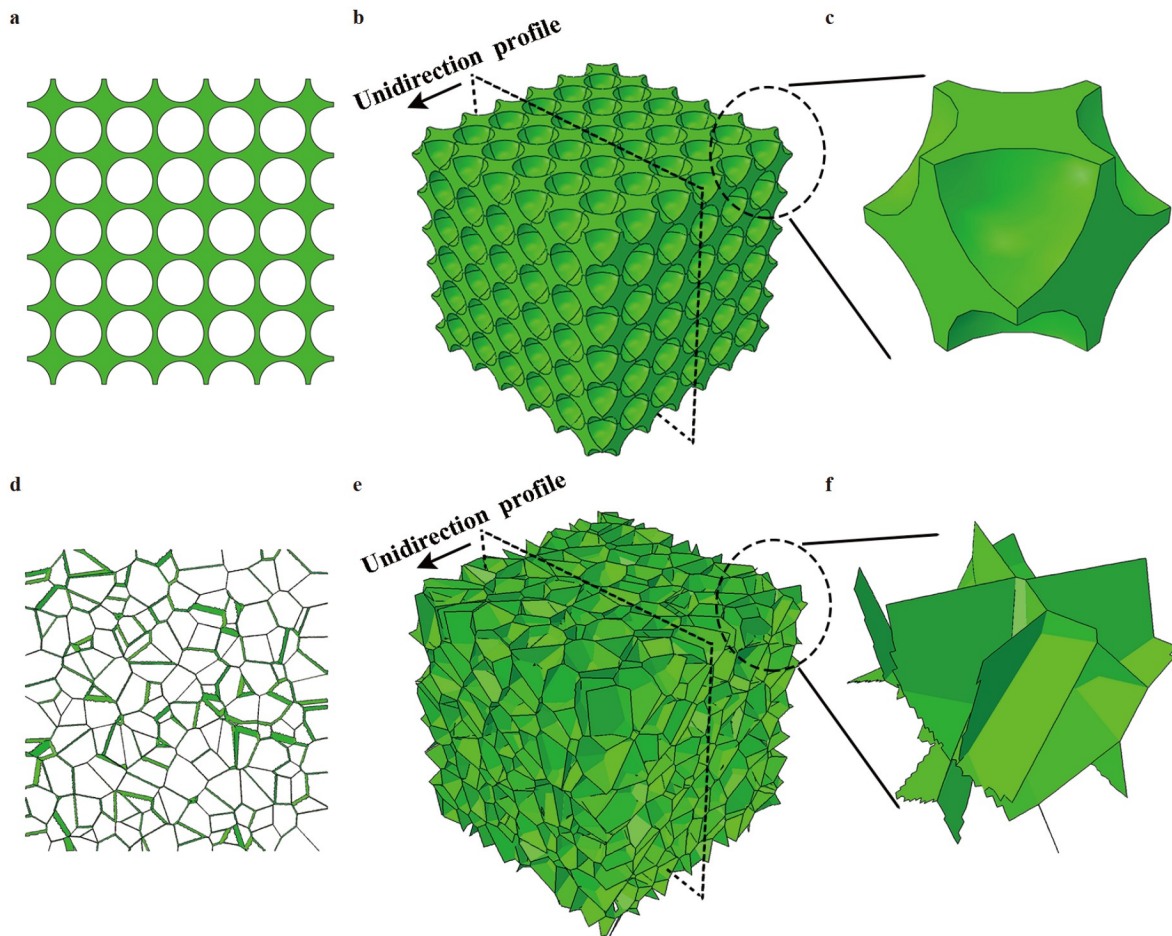

Figure 1   Sph-cell model: **a** unidirectional profile in *Y* direction; **b** whole model; **c** representative volume unit. The Voronoi model: **d** unidirectional profile in *Y* direction; **e** whole model; **f** representative volume unit.

and the initial yield surface of metal foams in the principle-strain space is very close, so it is less significant to study the subsequent yield evolution within the range of the failure surface. Similarly, the researches on subsequent yield surfaces are focused on overall compression conditions [6,7], corresponding to the "failure missing area" in Fig. 2c, and Wu et al. [50] gave the specific range of "failure missing area" on the basis of Voronoi model. Therefore, we verified the rationality of our theoretical model by triaxial loading conditions within "failure missing area", which is the permissible loading space. In Fig. 2c, the area composed of black points is the failure area, and the area composed of red points is "failure missing area". In the principle-strain space, only the loading conditions in the $\varepsilon_1 > \varepsilon_2 > \varepsilon_3$ space (The space between the $\varepsilon_1 = \varepsilon_2$ yellow plane and the $\varepsilon_2 = \varepsilon_3$ green plane) are considered because the models satisfy macroscopic isotropy, and the loading data in other spaces can be obtained by simple symmetry. Usually, different proportion loading conditions in the principle-strain space can be described by two dimensions, namely nominal strain triaxiality η_n and nominal strain Lode parameter ξ_n [19], the variables with subscript n represent the variables related to nominal strains or nominal stresses, and other variables without specifically noted are related to true strains or true stresses. The different latitude lines in Fig. 2c represent different η_n, which is defined as $\eta_n = \varepsilon_{en}/\varepsilon_{mn}$. And different longitude lines represent different ξ_n, which is defined as $\xi_n = 1 - \cos 3\theta = 1 - 4J_{3n}/\varepsilon_{en}^3$, ranging from 0 to 2, where θ is the Lode angle with the range between the two planes, J_{3n} is

the third invariant of the deviatoric nominal strain tensor, $J_{3n} = e_{1n}e_{2n}e_{3n}$. Since the "failure missing area" does not include overall tension conditions, it is better to set the compression directions to positive values in later characterization so that the calculated nominal strain triaxiality and nominal strain Lode parameter are also positive. In order to cover the permissible loading space, six η_n are selected, which are 0.067, 0.167, 0.22, 0.33, 0.417, 0.5, and five ξ_n are selected, which are 0, 0.46, 1, 1.54, 2, corresponding to the six red latitude lines and five black longitude lines in Fig. 2c, and together with the hydrostatic pressure condition, a total of 31 fixed-proportion loading conditions are preset for either mesoscopic model, which are indicated by red dots in the figure. For simplicity, we used the form of "(η_n, ξ_n)" to represent the loading condition, for example, "(0.33, 0)" represents the loading condition where the nominal strain triaxiality is 0.33 and the nominal strain Lode parameter is 0, and the corresponding triaxial nominal strain ratio is $\varepsilon_{1n} : \varepsilon_{2n} : \varepsilon_{3n} = 4 : 1 : 1$. In addition, "(0, *)" and "*" respectively represent the triaxial hydrostatic pressure condition and ξ_n of this condition, because all nominal strain Lode parameters coincide in the condition, which corresponds to that "(0, *)" is the coincide point of all longitude lines in Fig. 2c.

It is worth noting for uniaxial and biaxial loading conditions, at least one of three loading directions is the free boundary, and the stress on the free boundary is kept at 0, while the proportion of triaxial nominal strain changes significantly during the loading process due to the existence of
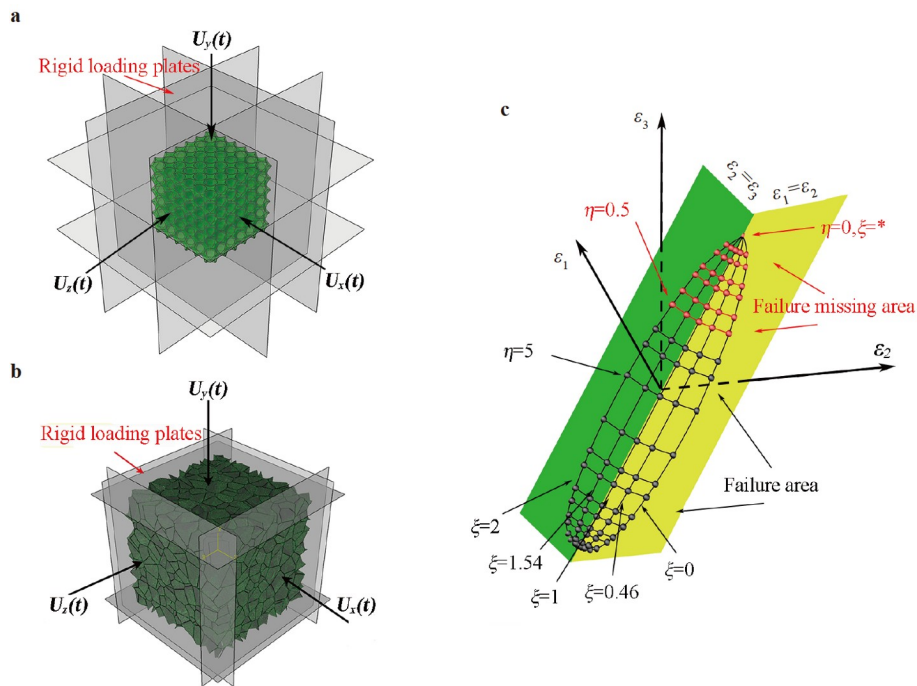
Figure 2 Schematic diagram of two mesoscopic models under the triaxial displacement-loading condition: **a** Sph-cell model; **b** Voronoi model. **c** Different loading conditions and the "failure missing area" in the principle-strain space.

Poisson's ratio. In other words, these loading conditions do not belong to fixed-proportion loading conditions in the principle-strain space, so the uniaxial and biaxial loading conditions are not considered here.

3.3 Reliability of mesoscopic model

After the loading data of different loading conditions were obtained, the two mesoscopic models should be validated and corrected. And the reliability verification of the mesoscopic model mainly includes experimental verification, isotropy verification and the correction of elastic modulus during the loading process.

3.3.1 Experimental verification
The reliability of Voronoi model had been verified by practical experiments in our previous researches [19], including uniaxial compression, uniaxial tension and biaxial tension experiments, and the verification results are good enough before the model failure (shown in Fig. 3). In addition, due to the uniformity and simplicity of internal structure, we considered that it does not need to carry out practical experimental verification on the Sph-cell model.

3.3.2 Isotropy verification
Since the cellular metals satisfy isotropy is the most im-

portant assumption in our theoretical model, we verified the isotropy of two mesoscopic models by the loading data, including the verification of uniaxial loading curves in different loading directions and the verification of plastic distortion-flexibility rates in different directions. The uniaxial loading curves in different directions of mesoscopic models are shown in Fig. 4a and b. We found that the coincidence of three curves of Sph-cell model is very high, while the three curves of Voronoi model are relatively close but do not overlap.

After that, we compared the coincidence of plastic distortion-flexibility rates during the triaxial loading process. From Eq. (6a), for any triaxial fixed-proportion loading condition, there are at least three plastic distortion-flexibility rates $\dot{C}_e$, which can be obtained from the stress and strain data in three directions, namely $\dot{C}_{ex}$, $\dot{C}_{ey}$, $\dot{C}_{ez}$. Therefore, the model is considered to satisfy isotropy when the equation $1/\dot{C}_{ex} = 1/\dot{C}_{ey} = 1/\dot{C}_{ez}$ holds. As shown in Fig. 4c, for Sph-cell model, the three $1/\dot{C}_e$ curves are close to completely overlapping into one curve, indicating that this model satisfies isotropy well during the triaxial loading process. And when the volumetric strain is smaller than 0.25, the $1/\dot{C}_e$ curves are basically straight lines. Combined with the unidirectional profiles during the loading process in Fig. 4e, it
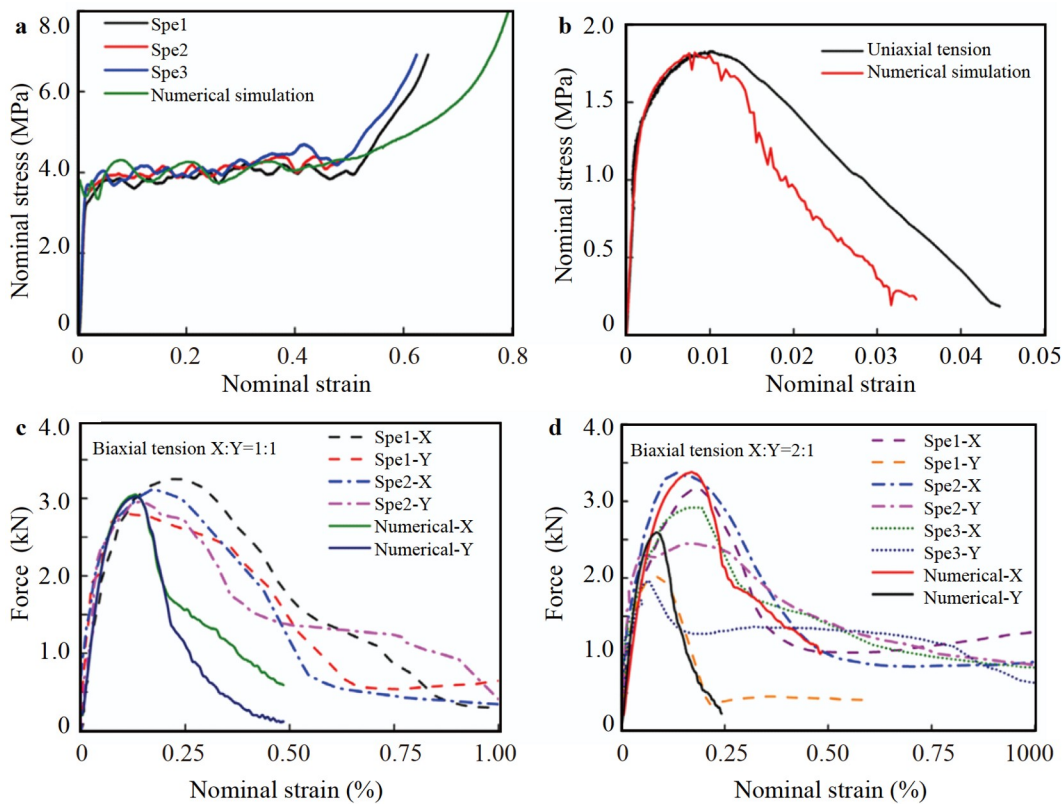
Figure 3 Comparison of simulation results and experimental results under different conditions [19]: **a** uniaxial compression condition; **b** uniaxial tension condition; **c** 1:1 biaxial tension condition; **d** 2:1 biaxial tension condition.

can be found that when the volumetric strain is smaller than 0.25, the hole shapes basically remain spherical corresponding to the straight-line segment in Fig. 4c, which indicates that the model deformation is dominated by shrinkage of hole structures. However, when the volumetric strain is greater than 0.25, the hole shapes begin to change and cannot remain spherical, which means the model deformation becomes dominated by the buckling and collapse of hole structures. Then, the hole structures disappear and the model is completely densification when the volumetric strain is about 0.45. Compared to Sph-cell model, the $1/\dot{C}_e$ curves of Voronoi model are not smooth and can barely be regarded as coincidence, as shown in Fig. 4d. From Fig. 4f, the model deformation during the loading process contains both local cell collapse and overall structure contraction, and the red dashed parts are the local cell collapse when the volumetric strain is 1.

Taken together, we believed that the Sph-cell model satisfies strong isotropy, but the isotropy of Voronoi model is slightly poor, so we considered to correct the isotropy of Voronoi model in the relevant characterization.

3.3.3 Elastic modulus correction

For isotropic non-dense metals, the current relative density [53] affects the constitutive relationship such as the yield stress and elastic modulus, and varies during the loading process. Considering the specific range of "failure missing area" and for convenience, we considered that the effect of the current relative density on elastic modulus can be represented by volumetric strain ε_m.

For Sph-cell model, there is a lack of relevant studies on the variation of elastic modulus with relative density, so we used the loading-unloading method to calculate the variation. Specifically, the model is loaded to different degrees and unloaded until triaxial stresses are 0 to obtain the triaxial stress differences and strain differences. Based on these differences and assuming the Poisson's ratio is essentially constant, the variation of elastic modulus with loading degrees can be obtained. And the points with different colors correspond to the data under different loading conditions, as shown in Fig. 5. Obviously, the variation of elastic modulus with volumetric strain can be divided into two sections according to the value of elastic modulus, the elastic modulus changes linearly with volumetric strain when the value is less than 70 GPa, and the linear equation of the elastic modulus of the Sph-cell model E_S corresponds to the black line in Fig. 5:

$$E_S = 88.356\varepsilon_m + 33.119 \text{ GPa.} \tag{16}$$
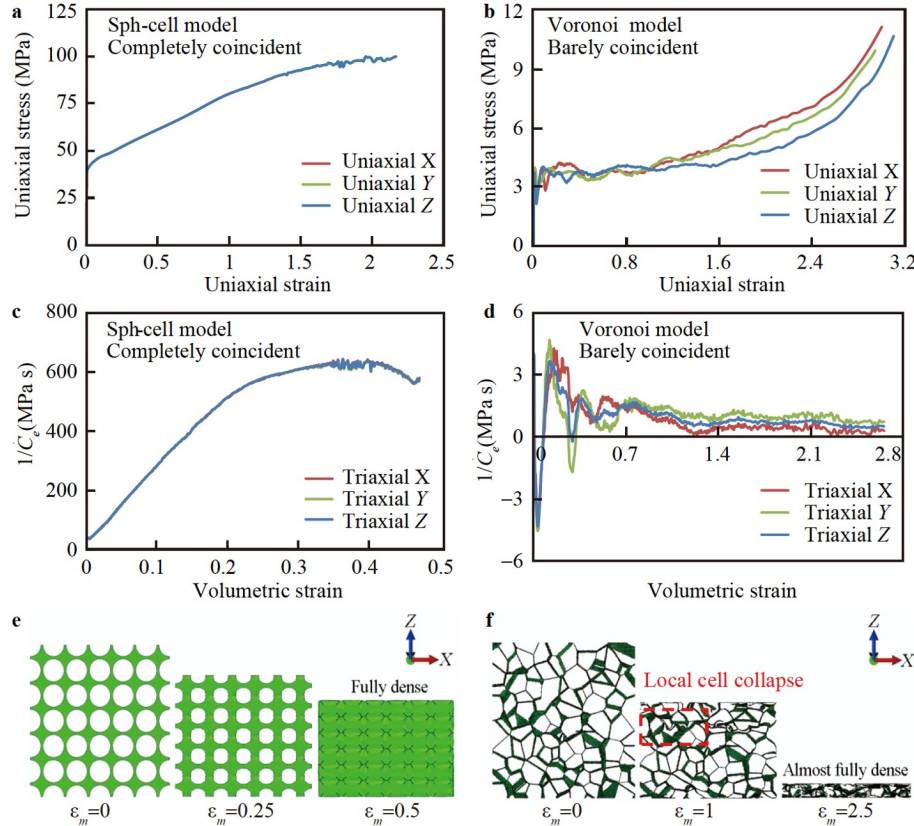
Figure 4 Isotropy verification of mesoscopic models. The uniaxial stress-strain curves in different directions: **a** Sph-cell model, **b** Voronoi model; $1/\dot{C}_e$ - ε_m curves in different directions under (0.5, 0) condition: **c** Sph-cell model, **d** Voronoi model; different profiles in Y direction under (0.5, 0) condition: **e** Sph-cell model, **f** Voronoi model.

Then, the elastic modulus keeps constant when the value is bigger than 70 GPa, this is because the E of matrix materials is 70 GPa (The red dotted line in Fig. 5).

For Voronoi model, the strain differences obtained by the loading-unloading method will bring large errors due to the complex internal structures, so we corrected the elastic modulus of Voronoi model by referring to related studies. Gibson and Ashby [1] proposed the classical formula for the variation of elastic modulus with relative density, Zhang et al. [49,52] gave the specific variation equation for Voronoi model based on GAZT model, so we replaced the influence of relative density in Zhang's study with ε_m to obtain the correction equation of elastic modulus of Voronoi model E_V, as Eq. (17):

$$E_V = 2.278\exp(1.15\varepsilon_m) \text{ GPa}. \tag{17}$$

Based on the data after correction, the $\bar{\sigma}$-$\bar{\varepsilon}^p$ relations under different loading conditions could be calculated according to Eqs. (7) and (11), the whole calculation process can be determined and shown in Appendix C.

3.4 Dispersion value

Further, for constitutive relations, the optimal undetermined parameters should minimize the dispersion degree of all curves. Therefore, to obtain the optimal dispersion degree and fitting coefficients, we defined the dispersion value R_{sum} to assess the dispersion degree, which is the sum of normalized standard deviations of the equivalent stresses for all loading conditions with equivalent plastic strain, as Eq. (18):

$$\bar{\sigma}_j^m = \frac{\sum\limits_{j=1}^{31} \bar{\sigma}_j}{31},$$

$$R_i = \sqrt{\sum\limits_{j=1}^{31}\left(\frac{\bar{\sigma}_j - \bar{\sigma}_j^m}{31\bar{\sigma}_j^m}\right)^2}, \tag{18}$$

$$R_{\text{sum}} = \sum\limits_{i=1}^{100} R_i,$$

where i represents the number of equal separations of equivalent plastic strain and j represents the number of different loading condition. $\bar{\sigma}_j$ is the equivalent stress for different loading conditions at the same equivalent plastic strain, and $\bar{\sigma}_j^m$ is the average value of $\bar{\sigma}_j$, R_i represents the dispersion value at the same equivalent plastic strain.

4. Results and discussion

According to the calculation process and the dispersion value, the optimal $\bar{\sigma}$-$\bar{\varepsilon}^p$ relations under different loading conditions can be obtained. Based on the results, we could not only compare our results with these of some known models, but also verify the characterization effect of the

constitutive equations in our theoretical model.

4.1 Optimal results and coefficients

The coefficients b and d affect the shape and dispersion degree of different $\bar{\sigma}$-$\bar{\varepsilon}^p$ relations, which can be determined by optimal R_{sum}. The optimal dispersion values and coefficients of the two mesoscopic models were listed in Table 3.

The $\bar{\sigma}$-$\bar{\varepsilon}^p$ relations are relatively concentrated during the whole loading process as shown in Fig. 6a and b. And in Fig. 6, the same colors are used for the same triaxiality curves, and the same thicknesses are used for the same Lode parameter curves. The results indicate that our theoretical model is applicable from initial yield to fully densification for isotropic cellular metals.

In addition, the relative density of initial dense metals is 100%, and the following equations hold

$$\varepsilon_m^p = 0, \ \dot{\varepsilon}_m^p = 0, \ \sigma_m \neq 0, \ \dot{C}_m = 0. \tag{19}$$

Substituting Eq. (19) into Eq. (11), we can get

$$\frac{ab}{c} = 1, \tag{20}$$

$$d = 0.$$

Combined with the coefficient values in Table 3 and Eq. (20), the coefficients b and d can be constructed as functions of initial relative density ρ_0, Eq. (21) exists
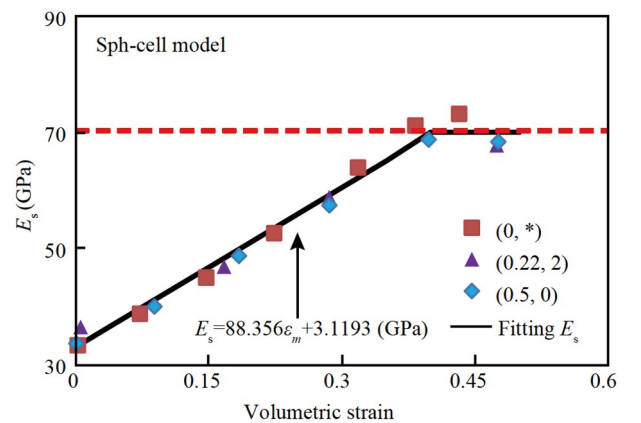
$$b = 2.13\rho_0 + 3.72,$$

$$d = 0.17\rho_0^2 - 0.422\rho_0 + 0.252. \tag{21}$$

Obviously, the parameter b increases with the increase of

Table 3 Optimal dispersion values and coefficients of mesoscopic models

Models	R_{sum}	a	b	c	d
Sph-cell	2.8	0.2	5	0.001	0.06
Voronoi	5.4	0.32	4	0.001	0.2

Figure 5 Variations of elastic modulus of Sph-cell model under different loading conditions.

initial relative density, and the coefficient d decreases with the increase of initial relative density.

## 4.2 Compared with several published theoretical model

4.2.1 Compared under preset loading conditions

Compared with the D-F model and the Zhu-Zheng model, for Sph-cell model, it can be calculated that the dispersion value obtained by the D-F model is $R_{sum} = 4.28$ and obtained by the Zhu-Zheng model is $R_{sum} = 4.73$, which are both larger than that of our theoretical model. And from Fig. 6c and e, it can be found that when the equivalent plastic

strain is about 0.25, the curves show a clear dispersion, and the dispersion occurs much earlier compared to Fig. 6a. For Voronoi model, the dispersion value obtained by the D-F model is $R_{sum} = 10.64$ and obtained by the Zhu-Zheng model is $R_{sum} = 10.81$, as shown in Fig. 6d and f, the dispersion degree in the second half in Fig. 6f increases significantly, and the dispersion degrees in Fig. 6d and f are greater than that in Fig. 6b. By above contrast, the relations between equivalent stress and plastic strain in our theoretical model have good consistency under all multiaxial loadings than these in the D-F model and the Zhu-Zheng model.

4.2.2 Compared under the extreme deformation process

Further, we compared the $\overline{\sigma}$-$\overline{\varepsilon}^{\,p}$ relations of different theo-
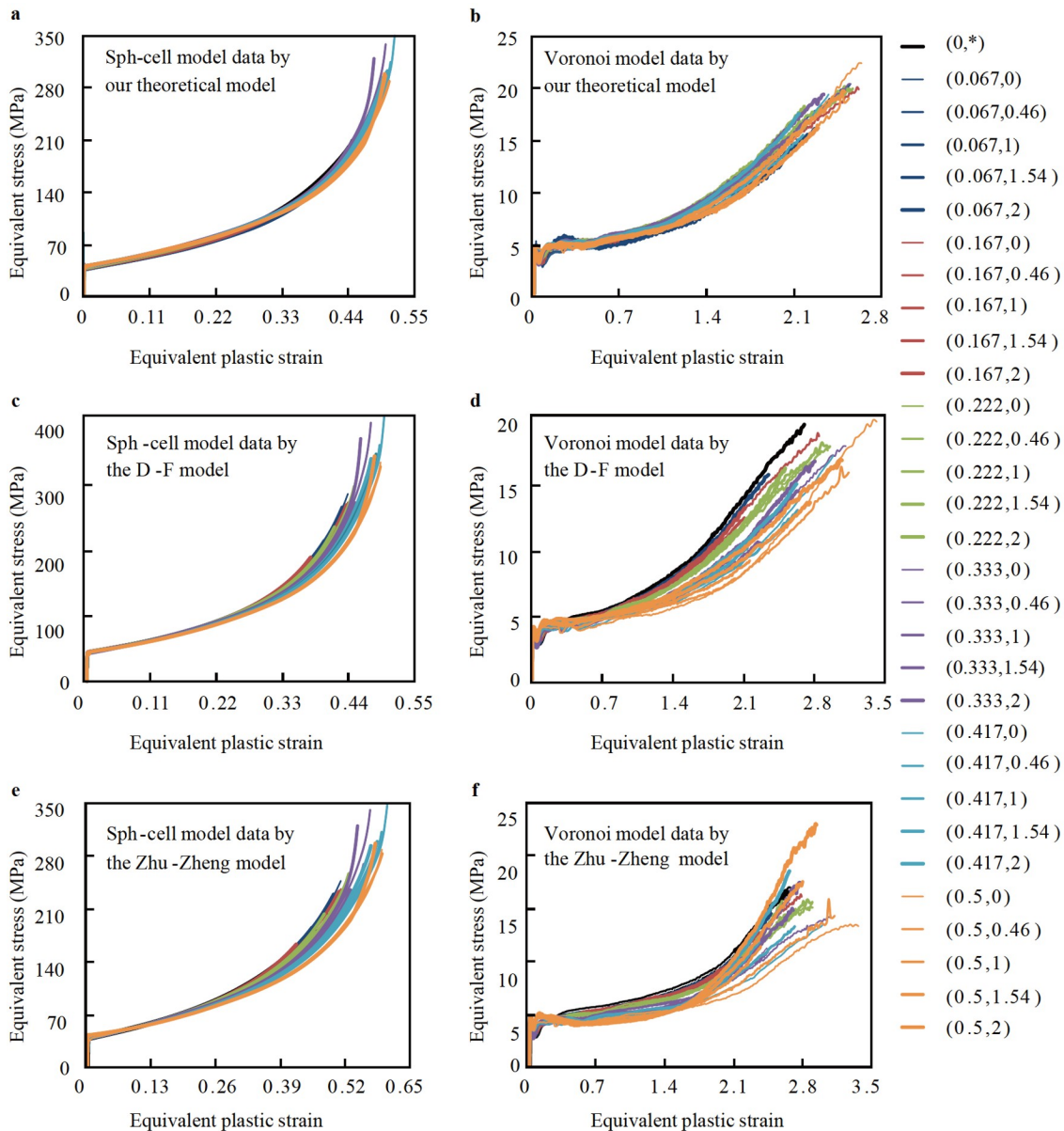
Figure 6 $\overline{\sigma}$-$\overline{\varepsilon}^{\,p}$ relations of mesoscopic models, by our theoretical model: **a** Sph-cell model, **b** Voronoi model; by the D-F model: **c** Sph-cell model, **d** Voronoi model; by the Zhu-Zheng model: **e** Sph-cell model, **f** Voronoi model.

retical models under the extreme deformation process designed in Sect. 2.4, as shown in Fig. 7. The fully dense points in the figure indicate the moment when the mesoscopic model is compressed to full densification. Obviously, after the fully dense points, the curves of the D-F model and the Zhu-Zheng model continue to increase sharply, but the curve of our theoretical model has clearly turned. Our curve produces some fluctuations due to contact stiffness and calculation errors. Overall, our curves after densification are closer to the performance of elasto-plastic dense metals under triaxial loading conditions than other models.

4.3 Characterization effect of two constitutive equations

4.3.1 Characterization effect of the constitutive equation characterized by equivalent stress and equivalent plastic strain

Based on the previous data, the characterization effects of the two additional equations in our theoretical model can be verified, which are Eqs. (13) and (14). The fitting curves of equivalent stress and equivalent plastic strain can be obtained based on Eq. (13) and shown in Fig. 8a and b for two mesoscopic models, the red points are the loading data and the blue points are the fitting data for all loading conditions, the goodness of fit corresponding to Sph-cell model is $R^2 = 0.994$, and the goodness of fit corresponding to Voronoi model is $R^2 = 0.976$. Combining the goodness of fit values and the two figures, it can be considered that Eq. (13) is reasonable enough.

4.3.2 Characterization effect of the constitutive equation characterized by plastic volume flexibility and plastic strain
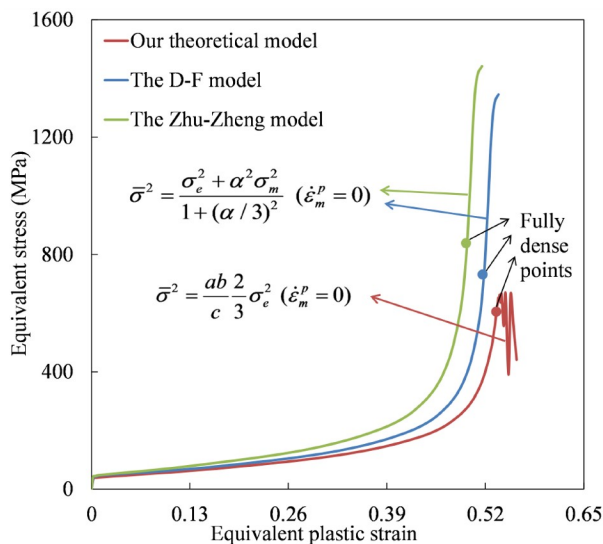
For the constitutive equation characterized by plastic vo-

lume flexibility and plastic strain, due to the poor isotropy of Voronoi model, we introduced the plastic Lode parameter (ξ^p) into the plastic volume-flexibility rate equation (Eq. (14)) for correction, and obtained the following equation:

$$\dot{C}_m = \frac{a_3 \dot{\varepsilon}_m^p}{1 + a_4 \varepsilon_m^p \exp\left[a_5 \left(\dfrac{\varepsilon_e^p}{\varepsilon_m^p}\right)^{a_6} \xi^p\right]}. \tag{22}$$

While there are four different variables in Eq. (22), so we select the fitting C_m as the horizontal axis of Fig. 8c and d, which makes the error look larger in the two figures. The goodness of fit corresponding to Sph-cell model is $R^2 = 0.995$ and to Voronoi model is $R^2 = 0.978$, we thought that the fitting results of Eq. (22) are acceptable for the two mesoscopic models. After the above analysis, it can be considered that the characterization effects of the constitutive equations are acceptable.

5. Subsequent yield surfaces

In order to determine whether the subsequent yield surfaces are self-similar, the topology of subsequent yield surfaces in the plastic principle-strain space was checked and analyzed.

For the reason of that the shape of the initial yield surface in the principle-strain space is more regular than that in the principle-stress space [19], it is recommended to use the equivalent plastic strain as the subsequent yield criterion, so the specific topology of subsequent yield surfaces in the plastic principle-strain space for the two mesoscopic models were drawn in Fig. 9a and b. For Sph-cell model, the shape of each subsequent yield surface appears to be fairly close to an ellipsoid, and for Voronoi model, the shapes of subsequent yield surfaces are close to ellipsoidal surfaces only when the equivalent plastic strain is less than 1.5.

In Refs. [7,9,30], the subsequent yield surfaces of metal foams are regarded as self-similar, but the self-similarity is not agreed in Refs. [6,31], and it is difficult to directly judge whether the self-similarity is satisfied from Fig. 9, so we fit the subsequent yield surfaces by the ellipsoidal equation, and compared the principal axis lengths of fitting ellipsoids. From Figs. 2c and 9, it can be found that the subsequent yield surface ellipsoids can be depicted by a standard ellipsoidal equation after a certain rotation of the plastic principle-strain coordinate system (ε_1^p, ε_2^p, ε_3^p) to the new coordinate system ($\varepsilon_1^{p'}$, $\varepsilon_2^{p'}$, $\varepsilon_3^{p'}$), shown in Fig. 10. And the new coordinates $\varepsilon_1^{p'}$, $\varepsilon_2^{p'}$, $\varepsilon_3^{p'}$ reflect the volumetric plastic strain, plastic Lord parameter, and Mises plastic strain respectively. The standard ellipsoidal equation in the new coordinate system is shown in Eq. (23).

Figure 7 $\overline{\sigma}$-$\overline{\varepsilon}^p$ relations of different theoretical models under the extreme deformation process.

$$\left(\frac{\varepsilon_1^{p'}}{\varepsilon_1^*}\right)^2 + \left(\frac{\varepsilon_2^{p'}}{\varepsilon_2^*}\right)^2 + \left(\frac{\varepsilon_3^{p'}}{\varepsilon_3^*}\right)^2 = 1, \tag{23}$$

where ε_1^*, ε_2^*, ε_3^* are the principal axis lengths of fitting ellipsoids. Then, we listed ε_1^*, ε_2^*, ε_3^* of different subsequent yield ellipsoids in Table 4, and the goodness-of-fit of all surfaces is greater than 0.97.

From Table 4, it can be determined that the proportions of the principal axis lengths for different subsequent yield ellipsoids are changed at different loading states for both mesoscopic models, implying that the subsequent yield surfaces are not self-similar.

6. Conclusion

Based on two accepted assumptions for isotropic non-dense metals, we proposed the new plastic flow theoretical model. In order to verify its rationality, we established two mesoscopic models with different initial relative densities and

different meso-structures. Then, the large amount of numerical simulation experimental data was established, which covers enough multiaxial loadings in the permissible principle-strain space, and the model verification and correction were carried out to ensure the validity of models and data. Then, the extreme deformation process from non-dense to dense state was designed, and the relations of equivalent stress and plastic strain in our theoretical model were

Table 4 Principal axis lengths of different subsequent yield ellipsoids

Models	$\bar{\varepsilon}^p$	ε_1^*	ε_2^*	ε_3^*
	0.05	0.0602	0.1328	0.0281
	0.15	0.3544	0.3828	0.0833
Sph-cell	0.25	0.5728	0.5748	0.1424
	0.35	0.7619	0.7634	0.1991
	0.45	0.9646	0.9681	0.2508
	0.5	0.9731	0.9731	0.2692
	1.0	5.55×10^3	3.48×10^6	0.5184
Voronoi	1.5	7.15×10^3	5.18×10^6	0.772
	2.0	1.78×10^3	5.41×10^6	1.026
	2.5	1.26×10^5	8.69×10^6	1.294
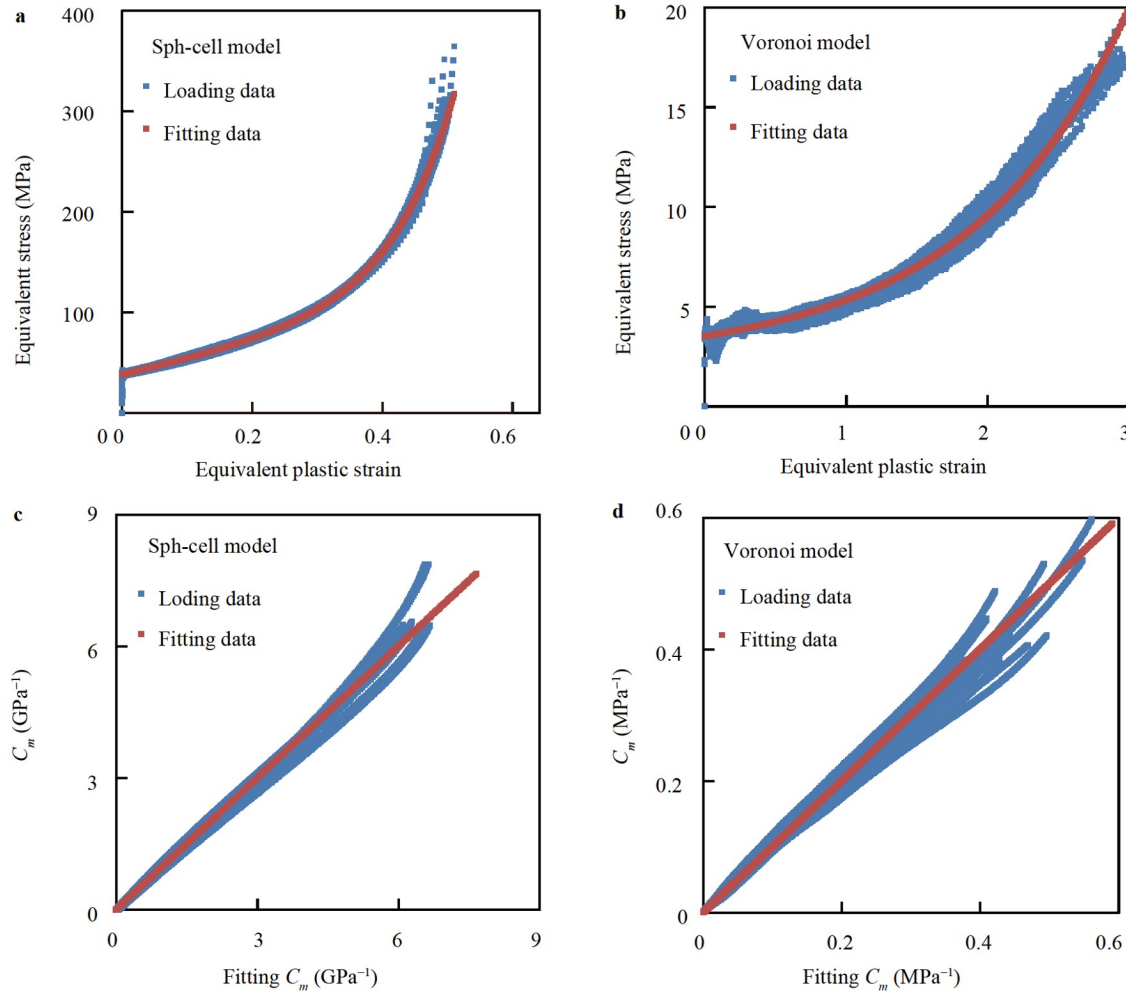
Figure 8 Fitting effect of two additional constitutive equations. The equation of $\bar{\sigma}$-$\bar{\varepsilon}^p$ relation: **a** Sph-cell model, **b** Voronoi model; The equation of C_m and plastic strain: **c** Sph-cell model, **d** Voronoi model.

D. Qiao, et al. Acta Mech. Sin., Vol. 39, 423085 (2023)

423085-15
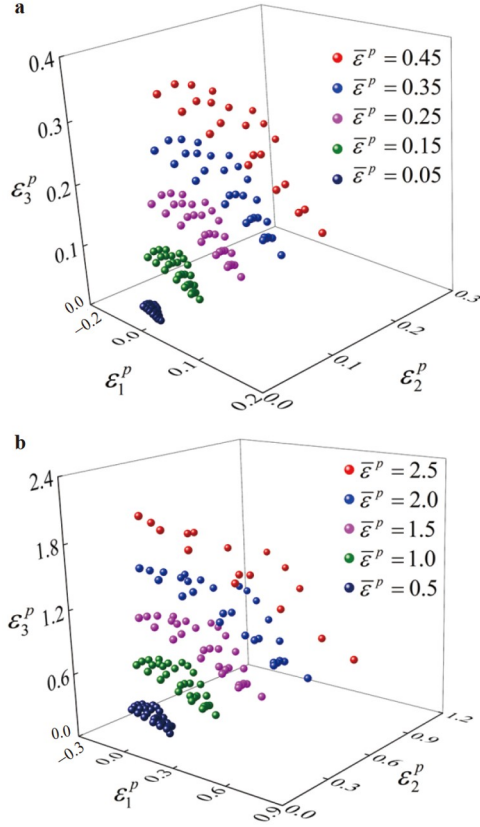
Figure 9 Subsequent yield surfaces in the plastic principle-strain space: **a** Sph-cell model; **b** Voronoi model.

compared with those in the D-F model and the Zhu-Zheng model. The research draws the following conclusions:

(1) Our theoretical model solves the controversies among current models and adapts the equivalent stress, equivalent plastic strain, and constitutive equations seamlessly to deformation from non-dense to dense state.

(2) Numerical results from two mesoscopic models show that the relations between equivalent stress and plastic strain in our theoretical model have good consistency under all multiaxial loadings than those in some known models.

(3) We checked the topology of subsequent yield surfaces in the plastic principle-strain space and the results turn out that the subsequent yield surfaces are not self-similar.

(4) A large amount of numerical simulative test data is provided, which not only well validates our theoretical model but also will be beneficial to the mechanical study of non-dense metals under multiaxial loadings.

Appendix A: Equation form of equivalent stress and equivalent plastic strain

For isotropic non-dense metals such as metal foams, different researchers gave different expressions for equivalent stress and equivalent strain, but these definitions of
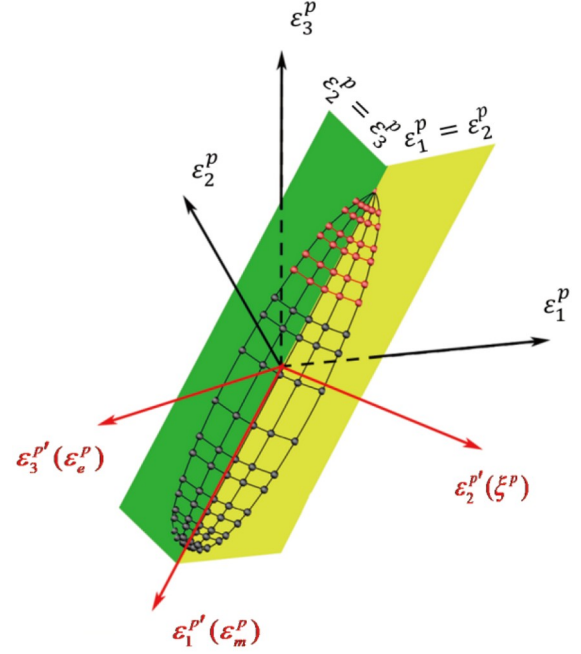
Figure 10 Two coordinate systems ($\varepsilon_1^{p'}$, $\varepsilon_2^{p'}$, $\varepsilon_3^{p'}$) and (ε_1^{p}, ε_2^{p}, ε_3^{p}) in the plastic principle-strain space.

equivalent stress and equivalent strain usually meet

$$P = \overline{\sigma}\dot{\overline{\varepsilon}}^{\,p}, \tag{A1}$$

where P is the plastic dissipation power representing the current state of materials, defined as Eq. (A2):

$$P = \dot{\boldsymbol{\varepsilon}}^p\boldsymbol{\sigma}. \tag{A2}$$

Combined with the extended Prandtl-Reuss equations, $\dot{\varepsilon}_{ij}^p$ can be written as

$$\dot{\boldsymbol{\varepsilon}}^p = \dot{\mathbf{e}}^p + \frac{\dot{\varepsilon}_m^p}{3}\boldsymbol{\delta} = \dot{C}_e\mathbf{s} + \dot{C}_m\frac{\sigma_m}{3}\boldsymbol{\delta}. \tag{A3}$$

If according to the definition $\dot{\varepsilon}_e^{\,p} = \sqrt{2\dot{\mathbf{e}}^p\dot{\mathbf{e}}^p/3}$, $\sigma_e = \sqrt{3\mathbf{ss}/2}$, and Eq. (6a) $\dot{\mathbf{e}}^p = \dot{C}_e\mathbf{s}$, there is $\dot{\varepsilon}_e^{\,p} = 2\dot{C}_e\sigma_e/3$. Therefore, substituting Eq. (A3) into Eq. (A2) leads to

$$P = \left(\dot{C}_e\mathbf{s} + \dot{C}_m\frac{\sigma_m}{3}\boldsymbol{\delta}\right)\boldsymbol{\sigma}$$
$$= \left(\frac{3}{2}\dot{\varepsilon}_e^{\,p}\mathbf{s}/\sigma_e + \frac{1}{3}\dot{\varepsilon}_m^{\,p}\boldsymbol{\delta}\right)\boldsymbol{\sigma} = \dot{\varepsilon}_e^{\,p}\sigma_e + \dot{\varepsilon}_m^{\,p}\sigma_m. \tag{A4}$$

In order to obtain the equivalent stress and equivalent plastic strain with clear physical significance, after replacing the stress or the strain rate in Eq. (A4) respectively, two forms of plastic power equations were deduced by transforming form:

$$1/\left(P\dot{C}_e\right) = \frac{2}{3}\sigma_e^2 + \sigma_m^2\dot{C}_m/\dot{C}_e, \tag{A5}$$

$$P\dot{C}_e = \frac{3}{2}\left(\dot{\varepsilon}_e^{\,p}\right)^2 + \dot{C}_e\left(\dot{\varepsilon}_m^{\,p}\right)^2/\dot{C}_m. \tag{A6}$$

The dimension of Eq. (A5) is the square of stress, and the

dimension of the second equation Eq. (A6) is the square of strain rate. After introducing a dimensionless function A, the equivalent stress and equivalent plastic strain can be defined as Eq. (A7):

$$(\overline{\sigma})^2 = AP/\dot{C}_e = A\left(\frac{2}{3}\sigma_e^2 + \sigma_m^2 \dot{C}_m/\dot{C}_e\right),$$

$$(\dot{\overline{\varepsilon}}{}^p)^2 = \dot{C}_e P/A = \frac{1}{A}\left[\frac{3}{2}\left(\dot{\varepsilon}_e^p\right)^2 + \dot{C}_e\left(\dot{\varepsilon}_m^p\right)^2/\dot{C}_m\right]. \tag{A7}$$

Appendix B: Equation of plastic volume flexibility of dense metals

The constitutive equation characterized by plastic volume flexibility C_m and plastic strain can be obtained by analogy with the equation form of plastic flexibility C.

The elastoplastic constitutive model of the initial dense metal is shown in Fig. B1, and the metal enters the plastic stage at moment t_0, σ_0 is the yield stress, ε_0 is the yield strain, so the following equations exist during the uniaxial loading process:

$$\varepsilon = \varepsilon(t), \quad \varepsilon_0 = \varepsilon(t_0),$$

$$\sigma = E_M\varepsilon_0 + E_M^*\left(\varepsilon(t) - \varepsilon_0\right), \quad t \geqslant t_0, \tag{B1}$$

where E_M is the elastic modulus and E_M^* is the hardening modulus of dense metals. Combined with Eqs. (B1) and (1b), the following Eqs. (B2) exists

$$\dot{C} = \frac{3}{2}\frac{\dot{\varepsilon} - \dot{\varepsilon}^e}{\sigma} = \frac{3}{2}\frac{\dot{\varepsilon} - \dot{\sigma}/E_M}{\sigma}$$

$$\Rightarrow \dot{C} = \frac{3\ddot{\varepsilon}(t)\left(1 - E_M^*/E_M\right)}{2\left[E_M\varepsilon_0 + E_M^*\left(\varepsilon(t) - \varepsilon_0\right)\right]}, \quad t \geqslant t_0. \tag{B2}$$

Appendix C: Calculation flowchart of the relations of equivalent stress and equivalent plastic strain

Based on the loading data, $\overline{\sigma}$-$\overline{\varepsilon}{}^p$ relations under different loading conditions could be calculated, so we took (0.33, 0) condition as an example to draw the flowchart of the whole calculation process. First, the triaxial stress-strain relations can be obtained as Fig. C1a, and the E of two models can be
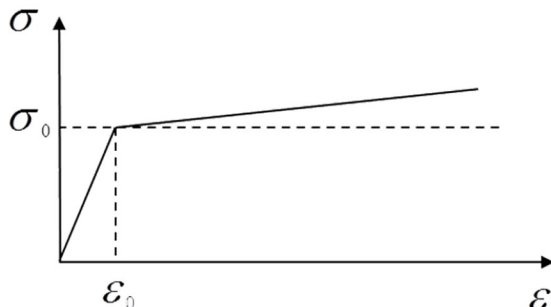
Figure B1 Elastoplastic constitutive model of the initial dense metal.

corrected by Eqs. (16) and (17). Then, σ_m-ε_m^p, σ_e-ε_e^p, $\dot{C}_m$-ε_m^p, $1/\dot{C}_e$-ε_e^p relations can be obtained by Eq. (7), shown in Fig. C1b. Finally, $\overline{\sigma}$-$\overline{\varepsilon}{}^p$ relations with different coefficients are given by substituting the results into Eq. (11), shown in Fig. C1c. According to the flowchart, we could obtain the $\overline{\sigma}$-$\overline{\varepsilon}{}^p$ relations under different loading conditions.

1 L. J. Gibson, and M. F. Ashby, Cellular Solids: Structure and Properties (Cambridge University Press, Cambridge, 1997).

2 N. S. Ha, and G. Lu, A review of recent research on bio-inspired structures and materials for energy absorption applications, Compos. Part B-Eng. **181**, 107496 (2020).

3 X. Zhang, L. Tang, Z. Liu, Z. Jiang, Y. Liu, and Y. Wu, Yield properties of closed-cell aluminum foam under triaxial loadings by a 3D Voronoi model, Mech. Mater. **104**, 73 (2017).

4 Z. Y. Xie, J. L. Yu, and Z. J. Zheng, A plastic indentation model for sandwich beams with metallic foam cores, Acta Mech. Sin. **27**, 963 (2011).

5 T. J. Lu, Ultralight porous metals: From fundamentals to applications, Acta Mech. Sin. **18**, 457 (2002).

6 C. Zhu, Z. Zheng, S. Wang, K. Zhao, and J. Yu, Modification and verification of the Deshpande-Fleck foam model: A variable ellipticity, Int. J. Mech. Sci. **151**, 331 (2019).

7 V. S. Deshpande, and N. A. Fleck, Isotropic constitutive models for metallic foams, J. Mech. Phys. Solids **48**, 1253 (2000).

8 L. J. Gibson, M. F. Ashby, J. Zhang, and T. C. Triantafillou, Failure surfaces for cellular materials under multiaxial loads—I. Modelling, Int. J. Mech. Sci. **31**, 635 (1989).

9 R. E. Miller, A continuum plasticity model for the constitutive and indentation behaviour of foamed metals, Int. J. Mech. Sci. **42**, 729 (2000).

10 M. Kepets, T. J. Lu, and A. P. Dowling, Mechanical characterization of the role of defects in sintered FeCrAlY foams, Acta Mech. Sin. **23**, 383 (2007).
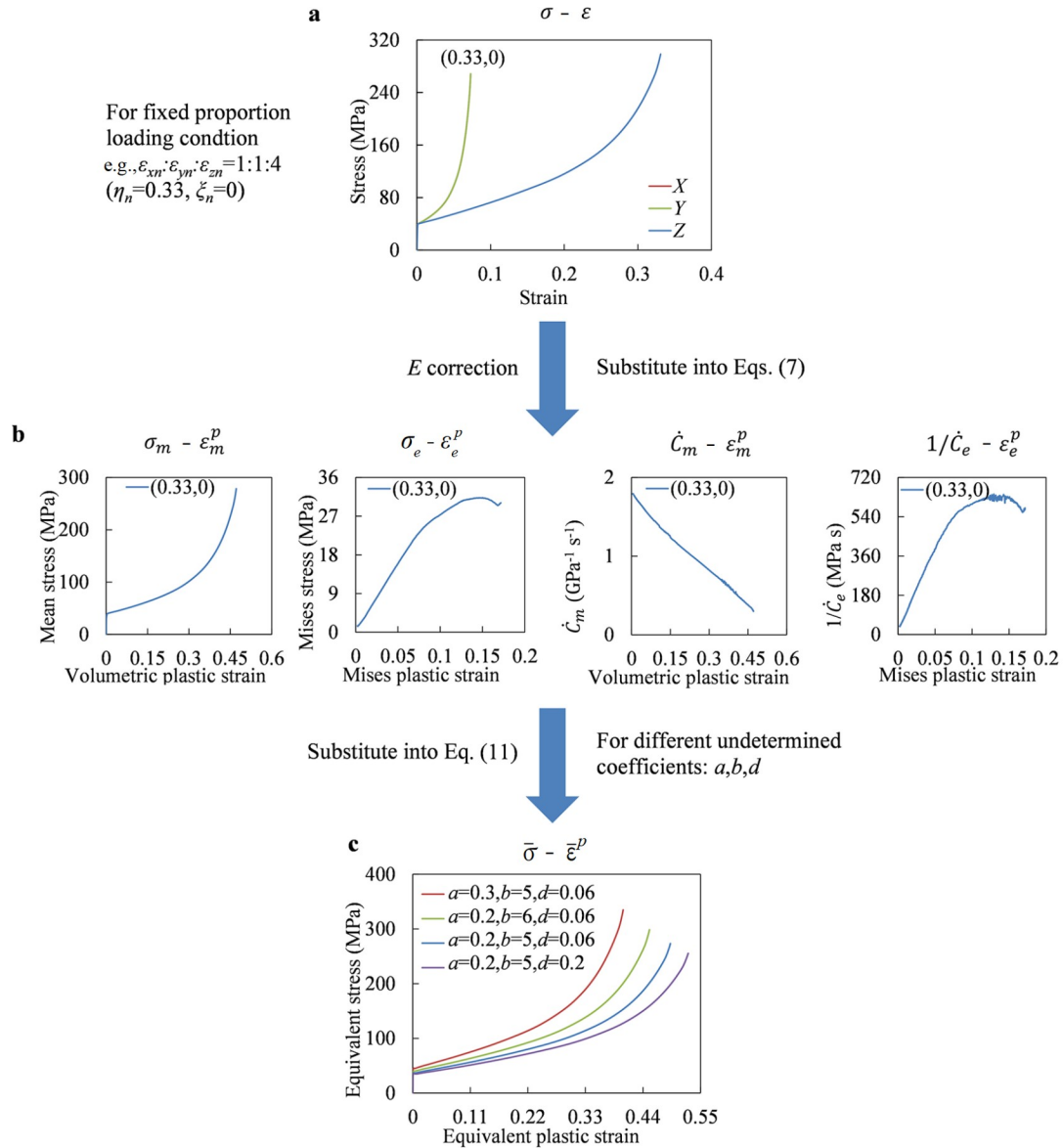
Figure C1　Calculation flowchart of the $\overline{\sigma}$-$\overline{\varepsilon}^p$ relations under (0.33,0) condition: **a** triaxial stress-strain relations in three directions; **b** σ_m-ε_m^p, σ_e-ε_e^p, $\dot{C}_m$-ε_m^p, $1/\dot{C}_e$-ε_e^p relations; **c** $\overline{\sigma}$-$\overline{\varepsilon}^p$ relations with different coefficients.

11　G. Luo, P. Xue, and S. Sun, Investigations on the yield behavior of metal foam under multiaxial loadings by an imaged-based mesoscopic model, Int. J. Mech. Sci. **142-143**, 153 (2018).

12　D. Ruan, G. Lu, L. Ong, and B. Wang, Triaxial compression of aluminium foams, Compos. Sci. Tech. **67**, 1218 (2007).

13　G. L. She, and H. X. Ding, Nonlinear primary resonance analysis of initially stressed graphene platelet reinforced metal foams doubly curved shells with geometric imperfection, Acta Mech. Sin. **39**, 522392 (2023).

14　G. Gioux, T. M. McCormack, and L. J. Gibson, Failure of aluminum foams under multiaxial loads, Int. J. Mech. Sci. **42**, 1097 (2000).

15　W. M. Huang, A simple approach to estimate failure surface of polymer and aluminum foams under multiaxial loads, Int. J. Mech. Sci. **45**, 1531 (2003).

16　Z. Zhou, Z. Wang, L. Zhao, and X. Shu, Loading rate effect on yield surface of aluminum alloy foams, Mater. Sci. Eng.-A **543**, 193 (2012).

17　Z. Zhou, Z. Wang, L. Zhao, and X. Shu, Uniaxial and biaxial failure behaviors of aluminum alloy foams, Compos. Part B-Eng. **61**, 340 (2014).

18　W. Zhuang, J. Sun, and D. Xie, Modified deshpande-fleck model considering a variable plasticity Poisson's ratio and a variable ellipticity, Adv. Mater. Sci. Eng. **2022**, 9235106 (2022).

19　Y. Wu, D. Qiao, L. Tang, Z. Liu, Y. Liu, Z. Jiang, and L. Zhou, Global topology of yield surfaces of metallic foams in principal-stress space and principal-strain space studied by experiments and numerical simulations, Int. J. Mech. Sci. **134**, 562 (2017).

20　H. E. Tresca, Mémoire sur l'écoulement des corps solides, Mém. Pres. Par. Div. Sav. **18**, 733 (1868).

21　B. de Saint-Venant, Sur l'établissement des équations des mouvements intérieurs operes dans les corps solides ductiles au delà des limites où l'élasticité pourrait les ramener à leur premier état, C. R. Acad. Sci. **70**, 473 (1870).

22　M. Lévy, Mémoire sur les équations générales des mouvements intérieurs des corps solides ductiles au delà des limites où l'élasticité pourrait les ramener à leur premier état, C. R. Acad. Sci. **70**, 1323 (1870).

23　R. V. Mises, Mechanik der festen Krper im plastisch- deformablen Zustand, Nachrichten von der Gesellschaften der Wissenschaften zu Göttingen, Mathematisch-Physikalische Klasse **1913**, 582 (1913).

24 L. Prandtl, Spannungsverteilung in plastischen: Proceedings of the First International Congress for Applied Mechanics, Delft, 1924.

25 A. Reuss, Berücksichtigung der elastischen Formänderung in der Plastizitätstheorie, Z. angew. Math. Mech. **10**, 266 (1930).

26 D. C. Drucker, and W. Prager, Soil mechanics and plastic analysis or limit design, Quart. Appl. Math. **10**, 157 (1953).

27 J. Zhang, Z. Lin, A. Wong, N. Kikuchi, V. C. Li, A. F. Yee, and G. S. Nusholtz, Constitutive modeling and material characterization of polymeric foams, J. Eng. Mater. Tech. **119**, 284 (1997).

28 M. F. Ashby, L. J. Gibson, U. Wegst, and R. Olive, The mechanical properties of natural materials, I. Material property charts, Proc. R. Soc. A **450**, 123 (1995).

29 T. C. Triantafillou, J. Zhang, T. L. Shercliff, L. J. Gibson, and M. F. Ashby, Failure surfaces for cellular materials under multiaxial loads—II. Comparison of models with experiment, Int. J. Mech. Sci. **31**, 665 (1989).

30 S. Forest, J. S. Blazy, Y. Chastel, and F. Moussy, Continuum modeling of strain localization phenomena in metallic foams, J. Mater. Sci. **40**, 5903 (2005).

31 C. Chen, and T. J. Lu, A phenomenological framework of constitutive modelling for incompressible and compressible elasto-plastic solids, Int. J. Solids Struct. **37**, 7769 (2000).

32 H. Fang, J. Bi, C. Zhang, M. Gutowski, E. Palta, and Q. Wang, A constitutive model of aluminum foam for crash simulations, Int. J. Non-Linear Mech. **90**, 124 (2017).

33 E. Combaz, C. Bacciarini, R. Charvet, W. Dufour, and A. Mortensen, Multiaxial yield behaviour of Al replicated foam, J. Mech. Phys. Solids **59**, 1777 (2011).

34 E. Combaz, C. Bacciarini, R. Charvet, W. Dufour, F. Dauphin, and A. Mortensen, Yield surface of polyurethane and aluminium replicated foam, Acta Mater. **58**, 5168 (2010).

35 H. Yang, J. Zhang, Z. Wang, Z. Wang, and Q. M. Li, Numerical study on the resistance of rigid projectiles penetrating into semi-infinite concrete targets, Acta Mech. Sin. **37**, 482 (2021).

36 W. Zhang, A. Tabiei, and D. French, A numerical implementation of the length-scale independent phase field method, Acta Mech. Sin. **37**, 92 (2021).

37 C. Pu, X. Yang, H. Zhao, Z. Chen, D. Xiao, C. Zhou, and B. Xue, Numerical study on crack propagation under explosive loads, Acta Mech. Sin. **38**, 421376 (2022).

38 R. Jia, and G. Zhao, Progress in constitutive models of aluminum foam (in Chinese), Chin. J. Theor. Appl. Mech. **52**, 20 (2020).

39 M. Vesenjak, T. Fiedler, Z. Ren, and A. Öchsner, Behaviour of syntactic and partial hollow sphere structures under dynamic loading, Adv. Eng. Mater. **10**, 185 (2008).

40 A. Öchsner, and G. Mishuris, Modelling of the multiaxial elasto-plastic behaviour of porous metals with internal gas pressure, Finite Elem. Anal. Des. **45**, 104 (2009).

41 E. Wang, G. Sun, G. Zheng, and Q. Li, Characterization of initial and subsequent yield behaviors of closed-cell aluminum foams under multiaxial loadings, Compos. Part B-Eng. **202**, 108247 (2020).

42 E. Wang, G. Sun, G. Zheng, and Q. Li, On multiaxial failure behavior of closed-cell aluminum foams under medium strain rates, Thin-Walled Struct. **160**, 107278 (2021).

43 L. Wang, K. Jiang, and D. Yang, Compression behavior of metal foams with real pore structures through CT scan images, J. Iron Steel Res. Int. **29**, 1886 (2022).

44 X. Zhang, L. Tang, B. Yang, H. Hu, and S. Tan, Study on the effect of the size irregularity gradient of metal foams on macroscopic compressive properties, Heliyon **8**, e12531 (2022).

45 X. Zhang, R. Wang, X. Li, C. Lu, Z. Wang, and W. Wang, Energy absorption performance of open-cell aluminum foam and its application in landing buffer system, J. Mater. Eng. Perform. **30**, 6132 (2021).

46 M. A. Kader, P. J. Hazell, A. D. Brown, M. Tahtali, S. Ahmed, J. P. Escobedo, and M. Saadatfar, Novel design of closed-cell foam structures for property enhancement, Addit. Manuf. **31**, 100976 (2020).

47 Z. Zheng, C. Wang, J. Yu, S. R. Reid, and J. J. Harrigan, Dynamic stress-strain states for metal foams using a 3D cellular model, J. Mech. Phys. Solids **72**, 93 (2014).

48 L. Tang, X. Shi, L. Zhang, Z. Liu, Z. Jiang, and Y. Liu, Effects of statistics of cell's size and shape irregularity on mechanical properties of 2D and 3D Voronoi foams, Acta Mech. **225**, 1361 (2014).

49 X. Zhang, Y. Wu, L. Tang, Z. Liu, Z. Jiang, Y. Liu, and H. Xi, Modeling and computing parameters of three-dimensional Voronoi models in nonlinear finite element simulation of closed-cell metallic foams, Mech. Adv. Mater. Struct. **25**, 1265 (2018).

50 Y. Wu, D. Qiao, L. Tang, H. Xi, Y. Liu, Z. Jiang, Z. Liu, and L. Zhou, Global topology of failure surfaces of metallic foams in principal-stress space and principal-strain space studied by numerical simulations, Int. J. Mech. Sci. **151**, 551 (2019).

51 L. L. Wang, and X. L. Dong, Talk about dynamic plasticity and viscoplasticity (in Chinese), Explosion Shock Waves **40**, 9 (2020).

52 X. Zhang, L. Tang, Z. Jiang, Z. Liu, Y. Liu, and D. Fang, Effects of meso shape irregularity of metal foam on yield features under triaxial loading, Int. J. Str. Stab. Dyn. **15**, 1540014 (2015).

53 L. L. Hu, X. Q. Huang, L. Q. Tang, and Y. P. Liu, Study on the plastic constitution and the energy-absorbing characteristics of aluminum foam, Key Eng. Mater. **274-276**, 235 (2004).

各向同性非密实金属的塑性流动理论模型及验证

乔丹, 杨宝, 蒋震宇, 周立成, 刘泽佳, 刘逸平, 汤立群

摘要 目前已有较多各向同性非密实金属(如泡沫金属、多孔金属和晶格金属等)的力学特性和本构方程的相关研究, 然而各种理论模型所呈现的后续屈服面仍存在较大争议, 并且它们尚未在许可加载空间得到充分验证. 我们基于各向同性非密实金属的两个基本假设, 提出了一种新的塑性流动理论模型. 为了验证该理论模型的合理性, 我们构建了两个不同相对密度和不同细观结构的仿真模型, 并在许可主应变空间中进行了大量数值模拟试验. 我们的理论模型解决了现有理论中存在的一些争议, 并且使得等效应力、等效应变和本构方程无缝地适应从非密实到密实状态的变形过程. 数值结果表明, 相比已知模型, 我们的理论模型得到的等效应力与等效塑性应变间的关系在多轴加载下具有更好的一致性. 此外, 我们还检查了塑性主应变空间中后续屈服面的拓扑结构, 发现不同后继屈服面之间并不满足自相似性. 本文中大量数值测试数据既验证了我们的理论模型的有效性, 同时也为研究非密实金属的多轴力学行为提供了重要依据.